AIAA JOURNAL
Vol. 32, No. 5, May 1994

Computational/Experimental Investigation of Staged Injection into a Mach 2 Flow

D. R. Eklund*
National Research Council, Hampton, Virginia 23681
D. G. Fletcher,† R. J. Hartfield Jr.,‡ and J. C. McDaniel§
University of Virginia, Charlottesville, Virginia 22903
G. B. Northam¶
NASA Langley Research Center, Hampton, Virginia 23681
and
C. L. Dancey** and J. A. Wang††
Virginia Polytechnic Institute and State University, Blacksburg, Virginia 24061

The staged normal injection of two jets of air into a Mach 2 freestream behind a rearward-facing step has been investigated using laser-induced iodine fluorescence and laser doppler anemometry techniques. A detailed data set has been compiled that includes profiles of pressure, temperature, two components of velocity, and mole fraction of the injectant at 44 locations, plus planar surveys of pressure, temperature, velocity, and mole fraction. A companion numerical study was performed using the SPARK Navier-Stokes code. Good overall agreement was observed for this complex, highly three-dimensional flowfield. Discrepancies were observed in the computed and measured total temperatures, turbulent mixing, and shock strengths. The effect of grid resolution was investigated by calculating solutions on grids of 60,000 points, 200,000 points, and 450,000 points. Differences in the solutions on the two finer grids were small. The effect of turbulence modeling was investigated by calculating solutions with three different algebraic models for the jet turbulence. Overall, the turbulence models were found to have the greatest effect on the numerical solutions, followed by the grid resolution and the injectant Mach number.

Nomenclature

c = eddy viscosity constant
d = jet diameter
$\bar{e}$ = mean difference
L = length scale
M = Mach number
N = number of points
P = pressure
T = temperature
U, V, W = mean velocity components in the x, y, and z coordinate directions, respectively
U_e = mean x component of velocity at boundary layer edge, $U(\delta_{99\%})$
u', v', w' = rms fluctuations about the U, V, and W velocity components, respectively
$u'w'$ = Reynolds stress component
x, y, z = cartesian coordinates
μ = coefficient of viscosity
ρ = density
χ = mole fraction of the injectant

Subscripts and Superscripts

c = calculated
m = measured
t = turbulent
0 = stagnation
∞ = freestream

Received May 18, 1993; revision received Nov. 5, 1993; accepted for publication Nov. 10, 1993.

*Research Associate; currently Research Associate, Analytical Services and Materials, Hampton, VA. Member AIAA.
†Graduate Research Assistant; currently Research Scientist, Experimental Fluid Dynamics Branch, NASA Ames Research Center, Moffett Field, CA 94035. Member AIAA.
‡Graduate Research Assistant; currently Assistant Professor, Department of Aerospace Engineering, Auburn University, Auburn, AL. Member AIAA.
§Associate Professor, Department of Mechanical and Aerospace Engineering. Member AIAA.
¶Senior Research Scientist, Experimental Methods Branch. Member AIAA.
**Assistant Professor, Department of Mechanical Engineering. Member AIAA.
††Graduate Research Assistant, Department of Mechanical Engineering.

Introduction

An important step in the validation of computational fluid dynamics (CFD) codes is modeling experiments of increasing complexity that have reliable and comprehensive data sets. Emerging nonintrusive measurement techniques that provide extensive in-stream data are potentially an invaluable tool in the validation process. Laser-induced iodine fluorescence (LIIF) techniques have been developed at the University of Virginia (UVA) for the experimental investigation of compressible flowfields. These nonintrusive optical techniques, which avoid the disturbances generated by the insertion of physical probes, have been calibrated at known flow conditions and provide detailed databases that can serve as benchmarks for CFD codes.

LIIF techniques were used to investigate the Mach 2 flow over a rearward-facing step with staged normal injection of two underexpanded air jets downstream of the step. It is a highly three-dimensional flow with many complex features: boundary layer separation, reattachment, curved bow shocks, shock-shear layer and shock-boundary layer interactions, jet-

induced counter-rotating vortices, and Mach disks. This flowfield represents the nonreacting flow through a unit supersonic combustor. Mach 2 combustor inlet flow corresponds to flight Mach numbers of 5–7, the low Mach number range for supersonic combustors. The rearward-facing step and the staged, or in-line, injectors were chosen to provide regions of recirculation for flameholding in the supersonic flowfield. Fuel injection in realistic combustors will utilize a combination of transverse and tangential geometries. Transverse injection is used predominantly at the lower Mach numbers because it provides good fuel penetration, mixing, and heat release, albeit at the expense of large total pressure loss. Tangential injection results in lower total pressure losses but also results in less fuel penetration. While transverse injection into a cross flow is a fundamental means of injecting fuel into a supersonic combustor, it has numerous other applications including thrust vectoring, impingement heat transfer, and atmospheric pollution.

Earlier investigations yielded a relatively sparse number of measurements. These measurements were useful, nevertheless, in a previous code validation study.[1] Recently developed techniques have provided much more extensive data.[2] The measurements included both pointwise and planar surveys of pressure, temperature, and velocity taken using separate LIIF techniques.[3-5] Additionally, a laser doppler anemometry (LDA) system, developed at Virginia Polytechnic Institute and State University, was used to obtain measurements of two components of velocity and their fluctuations to characterize the turbulence field.[6] These data provide a truly extensive test for three-dimensional, compressible CFD codes and have recently been used in a CFD code validation study[7] and a CFD code competition.[8] In this work, the flowfield was modeled with the SPARK code[9,10] that was developed at the NASA Langley Research Center. Because of the quantity of measurements taken, a statistical measure was used to help assess agreement.

This paper first outlines the extensive experimental data set that has been compiled. A brief description of the SPARK computer code, including details of the turbulence modeling and the computational solution technique, then follows. Finally, comparisons between the computational and experimental results are examined and discussed, and conclusions are drawn.

Experimental Technique

Experimental Conditions

The rectangular UVA test section is depicted schematically in Fig. 1, with the coordinate system indicated. The dimensions of the test section are given in terms of the jet diameter, $d = 1.93$ mm, in Table 1. A straight wall extended from the end of the nozzle contour to the step, with a 0.5-deg slope to allow for boundary-layer growth. Two circular air jets were placed 3.0 and 7.0 step heights downstream of the step on the tunnel centerline. The origin of the coordinate system is at the center of the first injector. The nominal flow conditions are also listed in Table 1. The one parameter in Table 1 which was

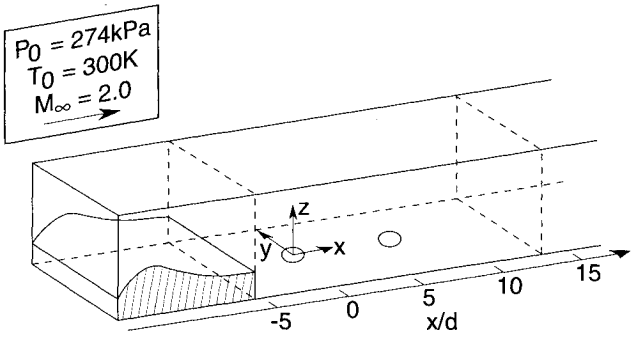

Fig. 1 Schematic of the UVA test section.

difficult to specify accurately was the jet exit Mach number. Measured jet exit Mach number values ranged from 1 to 1.35. The effect on the calculated flowfield from the uncertainty in the jet exit Mach number over this range will be examined in a later section. The freestream pressure, temperature, and U-velocity values given in Table 1 have been used to nondimensionalize all of the quantities presented in this paper.

Measurement Techniques

The majority of the measurements were made using laser-induced iodine fluorescence (LIIF) techniques developed at the University of Virginia. LIIF techniques are nonintrusive optical techniques that infer flowfield properties from signals resulting from the laser-induced fluorescence of iodine molecules seeded into the flow. In general, laser-induced fluorescence involves the absorption and subsequent radiation of photons by molecules that have transitions resonant with the laser excitation wavelength. The pointwise LIIF technique recorded a high-resolution portion of the iodine absorption spectrum using a scanning, narrow-band ring dye laser. Pressure and temperature were deduced from the lineshape. Velocity in the direction of the laser beam was determined from the frequency shift measured relative to an unshifted spectrum in a static iodine cell. A detailed description of this technique and its application is given in Refs. 2 and 3.

Planar LIIF (PLIIF) measurements were made using a 6-W, argon-ion laser whose beam was spread into a thin sheet. The planar fluorescence signal was imaged onto a 512×512 pixel charge-coupled device digital array camera. Separate techniques were developed operating the argon laser in both its broadband and narrow-band modes to obtain planar measurements of temperature, pressure, and U- and W-velocity components.[2,5] Additionally, planar injectant mole fraction measurements were made. In the planar mole fraction technique a ratio is taken between the signal obtained when only the injectant air is seeded with iodine and when the whole flow is seeded. After scaling the images to account for changes in the iodine seeding fraction between the two seeding conditions, the ratioed image provides an absolute measure of the mole fraction of the injectant at each location.[4]

Laser Doppler anemometry is a well-established technique for pointwise velocity measurements. The LDA system used was a two-component system, operated in an off-axis forward scatter mode. The LDA seed material was 0.54-μm polystyrene latex (PSL) spheres dispersed in ethanol. At each measurement location, 1024 measurements were made for the determination of the mean velocity and their fluctuations.[6] Because the LIIF and PLIIF techniques provide only time-averaged data, the LDA data was an important addition to the data set in providing information about the turbulence intensity in the flowfield.

Reference 2 provides a detailed description of the measurement uncertainty and spatial positioning error of the experimental techniques. The nominal uncertainty for the pressure, temperature, U-velocity, and V-velocity values obtained with the LIIF techniques were $\pm 4\%$, $\pm 2\%$, $\pm 5\%$, and $\pm 4\%$, respectively, as a percentage of the freestream conditions. The uncertainty for the pressure, temperature, U-velocity, W-velocity, and mole fraction values obtained with the PLIIF techniques were $\pm 6\%$, $\pm 5\%$, $\pm 2\%$, $\pm 6\%$, and $\pm 1.5\%$, respectively. Finally, the uncertainty for the mean and fluctuating components of velocity obtained with the LDA technique was $\pm 2\%$, while the uncertainty in the $u'w'$ values was $\pm 0.5\%$.

Experimental Data Set

Profiles of pressure, temperature, U velocity, and V velocity in the z direction were obtained using the LIIF technique at 44 locations within the flowfield, comprising a total of 382 individual measurement points. Data were taken at four y/d locations: 0.0, 0.5, 1.0, and 3.1 for each of eleven x/d locations: -1.0, 0.0, 1.5, 3.1, 4.6, 6.1, 6.6, 7.1, 8.1, 12.8, and

Table 1 Test section geometry and nominal operating conditions

Feature	Dimension	Parameter	Freestream	Injector exit
Test section height	$11.03d$	P_0	274 kPa	263 kPa
Test section width	$15.79d$	T_0	300 K	300 K
End of nozzle contour	$x/d = -10.65$	M_∞	2.0	1.0
Step location	$x/d = -4.94$	P_∞	35 kPa	139 kPa
Step height	$H = 1.65d$	T_∞	167 K	250 K
1st injector location	$x/d = 0.0$	U_∞	518 m/s	317 m/s
2nd injector location	$x/d = 6.58$	Mass flow rate	200 g/s	1.64 g/s

25.6. Planar LIIF measurements of the mole fraction were obtained at 35 crossflow planes and four streamwise planes ($y/d = 0.0$, 0.5, 1.0, and 3.0). Planar measurements of temperature, pressure, U velocity, and W velocity were also obtained at these same four streamwise planes. The LDA system was used to obtain profiles of U, W, u', w', and $u'w'$ in the z direction at nine stations along the centerline of the test section ($y/d = 0.0$) and at six stations away from the centerline at $x/d = 25.6$. Profiles were obtained one step height upstream of the step ($x/d = -6.58$) to characterize the test section inlet conditions (including the turbulence level). LDA measurements were also made in the x direction immediately above the two injectors ($z/d = 0.51$).

Numerical Technique

Computer Code

The computer code used in this study was one of the SPARK family of codes developed at the NASA Langley Research Center.[9,10] The particular SPARK code employed solves the full three-dimensional, unsteady, Reynolds-averaged Navier-Stokes equations together with appropriate species continuity equations. The algorithm employed in the calculations was the steady-state Cross-MacCormack algorithm developed by Carpenter.[11] The algorithm is derived by replacing the one-sided difference operators in MacCormack's predictor-corrector scheme with compact difference operators. The algorithm, while formally still second-order accurate in space and time, attains fourth-order spatial accuracy at steady state.

To distinguish between the injectant air and the freestream air, two species continuity equations were solved. One species equation was solved for the mole fraction of oxygen χ_{O_2} and a second species equation was solved for the mole fraction of the injectant χ_{inj}. The second species was given the thermodynamic properties of air. The conservation of mass statement

$$\chi_{O_2} + \chi_{N_2} + \chi_{inj} = 1 \tag{1}$$

was then used to obtain the mole fraction of nitrogen χ_{N_2}.

Turbulence Modeling

The nonreacting combustor flowfield modeled in this work was turbulent.[6] While the turbulent fluctuations were not resolved, their effect upon the mean flow was modeled by solving the Reynolds-averaged conservation equations. Averaging introduces additional unknowns, the Reynolds stresses, heat flux and mass flux terms, that represent the effect of the turbulent fluctuations upon the mean flow. Eddy viscosity turbulence models evaluate the turbulent stresses through the Boussinesq approximation, which relates the turbulent stresses to the mean rate of strain by a coefficient, called the eddy viscosity coefficient.

Analogous to molecular viscosity, the eddy viscosity coefficient μ_t is evaluated as

$$\mu_t = c\rho V_t L_t \tag{2}$$

where c is a constant and V_t and L_t are turbulent velocity and length scales that are properties of the flow. Three algebraic turbulence models, which evaluate the velocity and length scales from the mean flow, were considered in this work. There was no attempt to optimize the performance of the turbulence models by adjusting the constants in the models.

The first model used was the Baldwin-Lomax model[12] that has been used extensively for wall-bounded flows. The Baldwin-Lomax model bases the velocity scale on the distribution of vorticity and the length scale on the distance from the wall. The second model combined the Baldwin-Lomax model along the walls with a turbulence model for the jets based on Prandtl's mixing length model. This modeling was achieved by limiting the search for the length scale in the Baldwin-Lomax model to the height of the boundary layer at the entrance to the test section. The eddy viscosity was defined as the maximum of the eddy viscosities calculated from the two models. This approach was used in Ref. 13 to model the turbulence of a jet in a supersonic flow. The constant in the model, as given in Ref. 13, was $c = 0.02$. The length scale used in Prandtl's mixing length model was defined as the average of the half-width of the jet in the spanwise and normal directions within a crossflow plane. The concentration of the injectant was used to determine the half-width. The velocity scale was defined as the maximum vorticity at a streamwise location times the mixing length. (See Ref. 7 for further details of the implementation of the turbulence model.) The third model combined the Baldwin-Lomax treatment of the wall boundaries with a turbulence model for the jets based on Eggers' mixing length model, which was designed for free shear layer flows as detailed in Ref. 14. As implemented, this model was identical to the second model except for the constant and the velocity scale in the turbulence model for the jet. The velocity scale was defined as the velocity in the core of the jet, and the constant used was $c = 0.0164$ as given in Ref. 14.

In all calculations the turbulent Schmidt and Prandtl numbers were set to constant values of 0.5 and 0.9, respectively. Riggins et al.[15] noted that in the wake behind a bluff body and in the outer layer of a boundary layer it has been observed experimentally that the diffusion of mass is greater than the diffusion of momentum, thereby suggesting that the turbulent Schmidt number is less than unity in large portions of the near field and far field of a normal injector. Finally, the turbulent viscosity was limited to 1000 times the laminar viscosity in all calculations.

Computational Grids

The effect of grid resolution was investigated by increasing the resolution uniformly while keeping the stretching parameters constant. The dimension of the grids used in the staged jet calculations were $69 \times 21 \times 41$, $103 \times 31 \times 61$, and $137 \times 41 \times 81$ (x, y, and z, respectively). The domain extended 31 jet diameters downstream of the first injector in the streamwise direction and from the tunnel side wall to the centerline in the spanwise direction. Grid clustering in the streamwise direction was employed in the vicinity of the step, at the boundaries of the jets, and at the outflow boundary. Grid clustering was also employed at the centerline in the spanwise direction and at the top and bottom walls in the normal direction. The minimum grid spacing at the base of the step in the normal direction was 80, 50, and 36 μm for the three grids, respectively. The injectors were modeled with 13, 22, and 33 points, and the points were distributed to approximate a circular cross section.

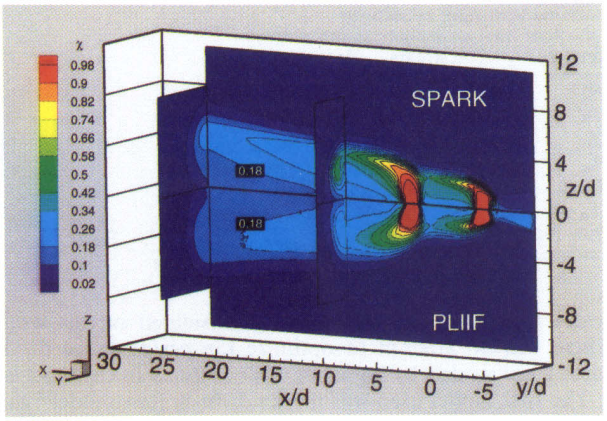

Fig. 2 Mole fraction contours of the injectant from the SPARK and PLIIF data.

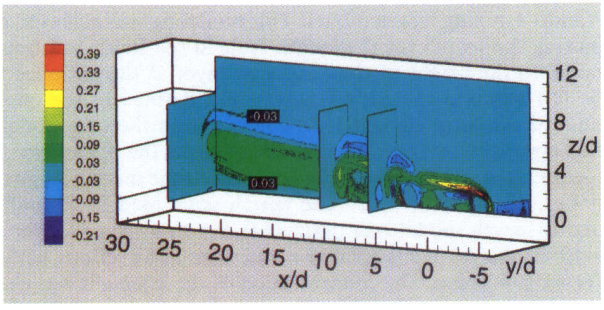

Fig. 3 Contours of mole fraction difference (interpolated SPARK values minus PLIIF data).

Boundary Conditions

A grid resolved Navier-Stokes calculation of the facility Mach 2 nozzle compared very well with measured values at a location one step height upstream of the step.[2] The calculated boundary layer thickness was approximately 1.6 mm or 0.51 step heights. The measured rms profiles compared favorably to other published measurements in fully developed and quasi-equilibrium turbulent boundary layers.[6] Spline fits of pressure, temperature, and velocity from the solution were used as the inflow boundary conditions. Symmetry boundary conditions were invoked at the injector centerline plane. They were applied by setting the V velocity equal to zero while imposing a zero normal gradient for pressure, temperature, and U and W velocities.

Along solid walls, the no-slip condition was imposed, together with assumptions of a zero normal pressure gradient and a zero normal total temperature gradient. However, the side tunnel wall was treated as an inviscid wall by setting only the normal velocity equal to zero. Neglecting to resolve the boundary layer on the side wall was not expected to appreciably affect the accuracy of the solution in the vicinity of the jets.

Conditions at the jet injection points were determined from the reservoir condition and the jet exit Mach number. The boundary layer at the exit of the jets, which was not measured, was neglected in the calculations. The conditions at the corner of the step were obtained by bilinear extrapolation from the three adjacent points in the normal and streamwise directions. Finally, the flow variables along the outer boundary were extrapolated from the interior assuming a zero gradient.

Iteration Technique

Initial solutions were started by setting the flow quantities in the domain equal to their values at the inflow plane. However, a linear velocity profile was assumed behind the step and the jet exit pressures were incremented gradually up to their experimental values. Coarse grid solutions were used as initial conditions for fine grid solutions. Similarly, a solution obtained with one turbulence model was used as the initial condition for a solution using a second turbulence model.

The solutions were advanced in time using a local time step calculated by combining the convective and the diffusive time scales as presented in Ref. 16. The Courant number and the artificial viscosity coefficient were set equal to 0.2 and 0.5, respectively, except for the staged jet calculations made on the fine grid which required the values of 0.1 and 0.6, respectively, for stability. (When using a global time step, the limiting Courant number was close to one.) A true steady-state solution was not attained. The residual, defined as the maximum change in the nondimensional density between successive iterations, typically dropped and then hovered near 10^{-2}. Within the recirculation zones behind the rearward-facing step and the injectors, the pressure was found to vary between 5–10%. Convergence was assessed by visual inspection of mole fraction contour plots, together with plots of mass conservation (conservation to within 0.5 % was attained). When the contour and mass conservation plots were unchanged between successive runs, the calculation was continued for an additional 2000 iterations, over which mean values were calculated to minimize the unsteadiness in the calculated flowfield. Plots of mean values obtained from successive runs of 2000 iterations were indistinguishable. Overall, between 10,000 and 30,000 iterations were required to attain this convergence. The corresponding processing time on a Cray-2 computer was approximately five hours for a solution on the coarse grid, 10–15 hours for a solution on the medium grid, and 40 hours for a solution on the fine grid.

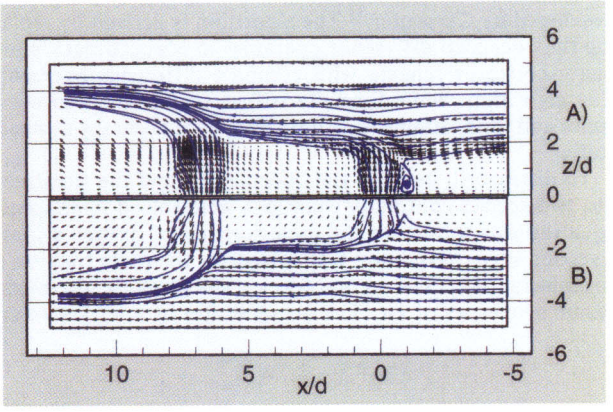

Fig. 4 Velocity vectors along the centerline of the test section from the a) SPARK and b) PLIIF data.

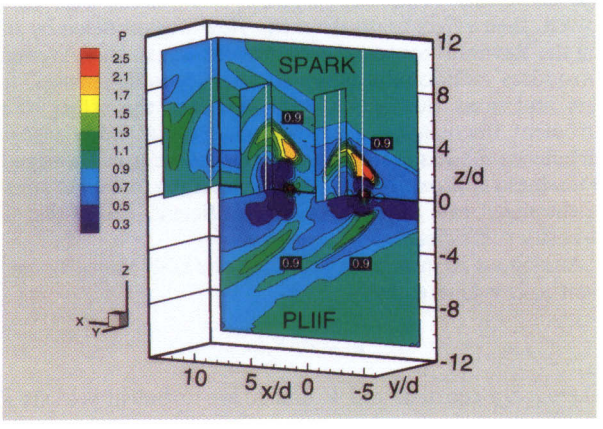

Fig. 5 Pressure contours from the SPARK and PLIIF data.

Results and Discussion

Comparisons with Planar Measurements

Figures 2–5 show comparisons between the planar data and the SPARK solution obtained on the medium grid using the Eggers turbulence model. Figure 2 shows comparisons of mole fraction contours in the centerline plane ($y/d = 0.0$) and in two crossflow planes ($x/d = 12.8$ and 25.6). The step and the two injectors are located at $x/d = -4.9$, 0.0, and 6.6, respectively. The PLIIF data have been reflected about the x axis in the figure. The computed and measured data exhibit generally good agreement. The calculated solution shows lower mole fraction values in the recirculation zone upstream of the first jet. The calculated solution is also marked by higher mole fraction values in the core of the injectant plume, as seen at the first crossflow plane. Agreement improves with downstream distance. The kidney shape of the injectant plume at the first crossflow plane is apparent. This characteristic shape of the plume is produced by a pair of streamwise vortices generated by the flow around both jets. The induced velocity field brings freestream fluid into the center of the injectant plume, creating the kidney shape that is associated with the transverse injection of underexpanded jets.[17,18] Interpolating the calculated mole fraction of the injectant in Fig. 2 to the experimental locations and then subtracting the measured mole fraction values from the calculated values yields the contour plot shown in Fig. 3. This figure, which includes a third crossflow plane ($x/d = 8.1$), highlights the differences between the SPARK and PLIIF mole fraction data. Higher mole fraction values are observed in the calculation (indicated by positive values) above the first jet and in the core of the injectant downstream of the second jet. Lower values in the calculation (indicated by negative values) are observed in the recirculation zone and in the periphery of the jet plume. The calculation predicts less mixing of the injectant. Apparently, the calculation underpredicts the extent of turbulent diffusion.

The velocity vectors and associated streamlines in the vicinity of the two injectors along the centerline plane ($y/d = 0.0$) are shown in Fig. 4. The measured vectors at every eighth pixel from the PLIIF image in the x and z directions are shown together with the calculated vectors at every other z grid location. This planar velocity field shows the very complex nature of the flowfield. Away from the injectors the main flow is seen to be turned toward the first injector by the expansion fan centered at the step. Near each injector, the flow is alternately turned away from the bottom wall ($z/d = 0.0$) by the oblique bow shock and then turned back to the wall by expansion waves. Note the extremely large velocity gradients that exist in this plane of the flowfield. For example, in the high shear region between the first jet and the recirculation zone, the velocity changes from approximately 175 m/s toward the wall to greater than 500 m/s away from the wall in less than 1 mm. The plot also indicates that the flow along the extended centerline of the first injector ($x/d = 0.0$) continues normal to the injection exit plane all the way to the end of the jet core. However, the streamlines from the center of the second jet ($x/d = 6.6$) exhibit downstream deflection. This will be seen later to be consistent with a larger pressure gradient in the x direction across the second jet than across the first. The velocities downstream of the two jets are predominantly away from the wall. This is due to the streamwise vortices that are generated by the interaction of the main flow with the transverse jets and is the origin of the kidney-shaped mole fraction contours in the crossflow plane that were observed in Fig. 2. As illustrated in the velocity vector plot, the major features of the centerline flowfield are in good agreement between the SPARK solution and the PLIIF data: the velocities in the recirculation zone, the penetration and orientation of the two jets, the deflection of the freestream by the bow shocks and expansion waves, and the velocities behind the two jets resulting from the streamwise vortices.

The pressure fields from the PLIIF measurements and the SPARK solution are shown in Fig. 5. (The white vertical lines show the positions where comparisons with the pointwise LIIF measurements will be made in the next section.) The first injector flow compresses across a strong shock (Mach disk) at the end of the jet core. It also generates a well-defined bow shock wave that extends into the main flow and is weakened by interaction with the expansion fan from the step and the expansion waves behind the first bow shock. Note the curved bow shocks indicated in the crossflow planes from the SPARK solution. At the last cross plane ($x/d = 12.8$) the calculated shock system associated with the second jet approaches the side wall and interacts with the shock system generated by the first jet that has reflected off of the side wall. Note also the greater pressure gradient in the x direction across the second jet that produced the downstream deflection of its streamlines seen in Fig. 4. The position of the prominent flow features along the centerline, as seen in Fig. 5, again are in good agreement; however, the shock systems are significantly stronger in the numerical solution.

Comparisons with Pointwise Measurements

Combining profiles from the mole fraction measurements, which have the lowest experimental uncertainties of the planar data, with the pointwise LIIF data provides a set of pressure, temperature, U-velocity, V-velocity, and mole fraction profiles at 44 locations. The effect of the grid resolution was examined by making calculations on three grids using the Eggers turbulence model. Due to space limitations, comparisons between the three calculations and the measurements will be shown only at the five stations indicated in Fig. 5. Figure 6 shows comparisons at the midplane of the first jet ($x/d = 0.0$, $y/d = 0.0$), which have been augmented by LDA U-velocity data at this station. Note that the last measurement made with the pointwise technique at this and the subsequent stations corresponds to $z/d = 5.83$. Hence, although the computational domain extended from the bottom wall to the top wall ($z/d = 11.03$), only the bottom 3/4 of the domain ($z/d \leq 8$) is shown in the figures. The expansion of the underexpanded jet occurs between the jet exit ($z/d = 0$) and $z/d \approx 1$. Excellent agreement is observed regarding the value of the minimum pressure for the expanding jet. The Mach disk is located

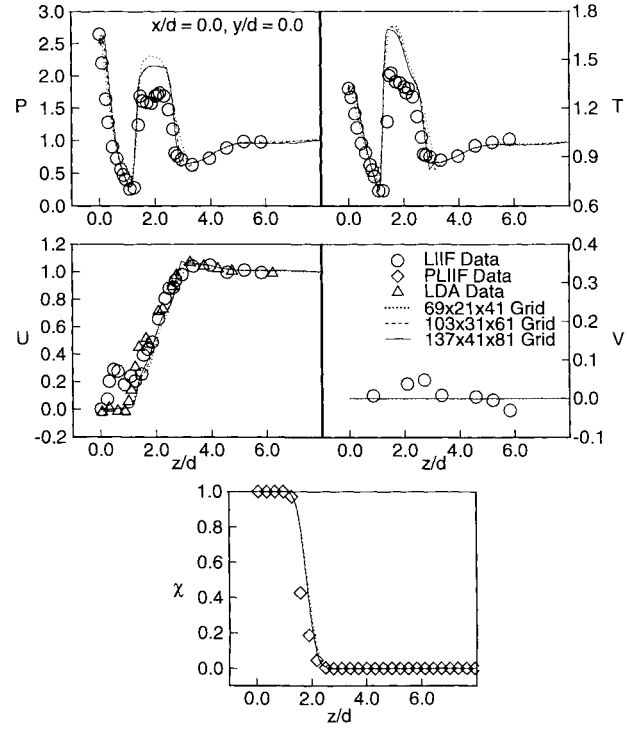

Fig. 6 Profiles of calculated values and pointwise LIIF measurements at $x/d = 0.0$, $y/d = 0.0$.

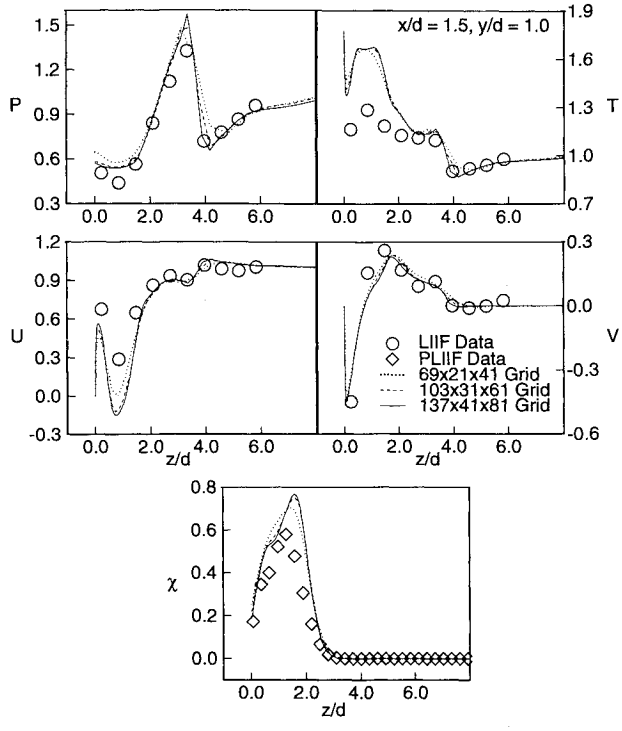

Fig. 7 Profiles of calculated values and pointwise LIIF measurements at $x/d = 1.5$, $y/d = 1.0$.

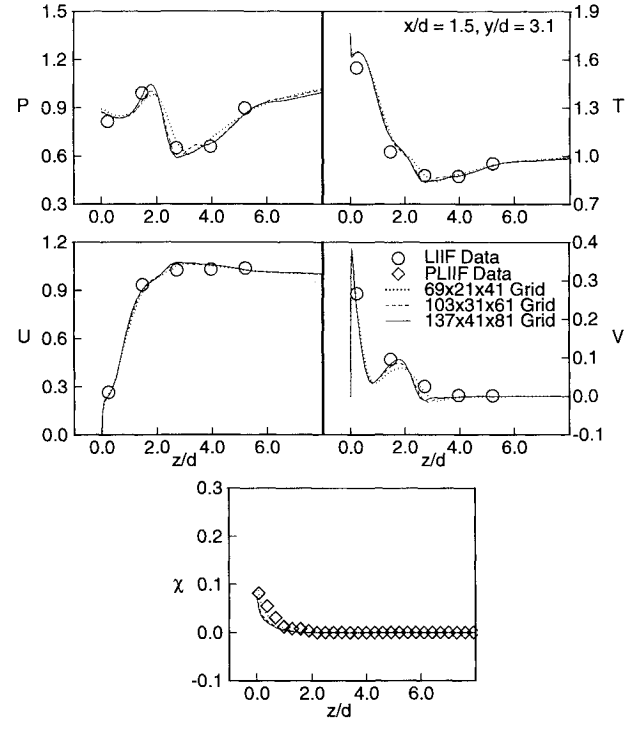

Fig. 8 Profiles of calculated values and pointwise LIIF measurements at $x/d = 1.5$, $y/d = 3.1$.

between $z/d \approx 1$ and $z/d \approx 1.5$, and the curved bow shock is encountered between $z/d \approx 2.5$ and $z/d \approx 3$. Separating the bow shock and the Mach disk is a relatively constant pressure region (located between $z/d \approx 1.5$ and $z/d \approx 2.5$). The expansion fan emanating from the corner of the step extends from $z/d \approx 3$ to $z/d \approx 5$. The grid sensitivity is small at this location, although grid refinement is observed to reduce the calculated pressure behind the Mach disk ($z/d \approx 1.5$). Nevertheless, the peak calculated pressure behind the Mach disk is larger than the LIIF value by approximately 41% of the freestream pressure. Similarly, the peak calculated temperature behind the Mach disk exceeds the corresponding measured value by 30% of the freestream value. (These trends were consistently observed in the solutions from the JANNAF CFD competition which employed different Navier-Stokes codes, computational grids, and turbulence models.[8]) The U-velocity values exhibit good overall agreement. Near the jet exit, the numerical solutions predict a negligible U-velocity component upstream of the Mach disk ($z/d \leq 1$), as supported by the LDA data (and observed in the PLIIF velocity data in Fig. 4). The U-velocity component measured with the pointwise LIIF technique, however, is as large as 28% of the freestream value, or 165 m/s. These large LIIF U velocities near the jet exit may result from a spatial positioning error in this high-gradient region of the flowfield. The V-velocity components measured by the LIIF technique are essentially zero, as expected for the flow symmetry plane. The mole fractions are in reasonably good agreement, although the calculations indicate slightly greater penetration, as observed in Figs. 2 and 3.

Figure 7 shows comparisons at the second station that is located 1.5 diameters downstream of the first jet and one diameter away from the centerline ($x/d = 1.5, y/d = 1.0$). At this station the compression waves originating from the Mach disk are centered at $z/d \approx 2.5$, the bow shock is centered at $z/d \approx 3.75$ and the expansion fan emanating from the step is centered at $z/d \approx 5$ (see also Fig. 5). The tendency for the coarse grid solution to smear out gradients, especially in the pressures, is evident in the profiles in Fig. 7. Agreement in the position of the bow shock improves with grid resolution at this location. The sensitivity to grid resolution decreases with succeeding refinements, as expected. Significantly higher temperatures are calculated within the low-momentum region near the wall ($z/d \leq 1$). The total temperature T_0, which is defined as

$$T_0 = T + \frac{\gamma - 1}{2} M_\infty^2[(U^2 + V^2 + W^2) + (u'^2 + v'^2 + w'^2)] \quad (3)$$

and equals 1.8 (nondimensional) for both the freestream flow and the injectant flow, provides another point of comparison between the LIIF and SPARK data. T_0 at the second measurement location ($z/d = 0.86$) inferred from the temperature and U- and V-velocity values is only 1.37 for the LIIF data compared to approximately 1.69 for the SPARK solutions. Several possible causes for this discrepancy will be discussed in the next section. Agreement in the U velocities is reasonably good except for lower calculated velocities near $z/d = 0.86$. The expansion of the first jet provides a greater disturbance to the surrounding fluid at $z/d = 0.86$ than at $z/d = 0.23$, deflecting more of the fluid. This accounts for the decrease in the measured and calculated U velocity near $z/d = 0.86$. As indicated by the V-velocity values, the agreement regarding the position and the strength of the vortex generated by the first jet is quite good. Finally, lower peak mole fraction values are measured at this station, indicating a greater extent of mixing at this location in the measurements.

The third station is located at $x/d = 1.5$, $y/d = 3.1$, which is positioned two diameters across from the previous station. Figure 8 shows the comparisons at this station. The attenuated compression waves originating from the Mach disk and the bow shock are centered at $z/d \approx 1.5$ and 2.5, respectively. The expansion fan is centered at $z/d \approx 4.5$. Agreement regarding the V velocities within the vortex generated by the first jet is again good. Excellent overall agreement between the measurements and the calculations is observed at this station. In general, comparisons at three diameters away from the centerline, where the gradients are less severe, were found to be very favorable.

The last two stations chosen for comparison lie downstream of the second jet. The fourth station is located one diameter away from the centerline and 1.5 diameters downstream of the

second jet ($x/d = 8.1$, $y/d = 1.0$). This station is in the same position relative to the second jet that the second station was to the first jet. Comparisons are shown in Fig. 9. As seen in the pressure profile, the compression waves originating from the Mach disk and the bow shock generated by the second jet are centered at $z/d \approx 3.5$ and $z/d \approx 5$, respectively (see also Fig. 5). The compression across the bow shock is seen to sharpen as the grid is further resolved, which, surprisingly, worsens the agreement with the measured pressures. The bow shock generated by the first jet crosses this profile at $z/d \approx 7.0$. The region within the jet plume ($z/d \leq 4$) is marked in both the calculations and the measurements by higher temperatures and lower U velocities than their respective freestream values. This plume region is broader than observed at the second station, owing to the greater penetration of the second jet, and exhibits higher U velocities and lower temperatures than seen in this region in Fig. 7. Very good agreement is again observed in the V-velocity values. Because of the deflection of the freestream by the first jet, the two streamwise vortices generated by the second jet are broader than the vortices generated by the first jet, as is indicated by a larger region of negative V velocities at this station than at the second station (cf. Fig. 7). The second jet also penetrates farther than the first jet, which results in a higher position for the peak mole fraction than at the second station. Figure 9 shows very good overall agreement in the mole fraction values at this station. The mole fraction values obtained from the solution on the coarse grid, which yields greater numerical diffusion, are actually in better agreement with the measurements.

The fifth station is located at $x/d = 12.8$, $y/d = 1.0$, which is approximately 4.5 diameters downstream of the previous station. Figure 10 shows the comparisons at this station. The weakened shock system associated with the second jet is located between $z/d \approx 5$ and $z/d \approx 8.5$. Note that the pressure below the shock system generated by the second jet ($z/d \leq 5$) is not constant. The pressure values are in good agreement at this station. Again, the effect of grid refinement decreases with succeeding refinements. Higher calculated temperatures are observed near $z/d = 2.5$, which reflect the higher temperatures calculated behind the second injector (as seen at the previous station) and the smaller level of turbulent mixing in the calculated solutions as indicated in the mole fraction profiles. The velocities are in relatively good agreement. Note that the U velocity in the core of the injectant has decreased from the value at the previous station. The position of the vortex, as reflected in the V velocities, is slightly higher in the calculations than in the measurements. Finally, at the center of the injectant, $z/d = 2.1$, the LIIF measurements again indicate a deficit of total temperature. The nondimensional total temperature inferred from the LIIF temperature and velocity measurements is approximately 1.46 vs 1.69 from the calculated values.

Because of the abundance of data, statistical measures were investigated to help assess agreement between experimental and calculated values. The derived quantity used is the mean difference of the nondimensional properties $\bar{e}$. It is obtained by first interpolating the calculated values to the experimental grid locations using linear interpolation. The mean difference

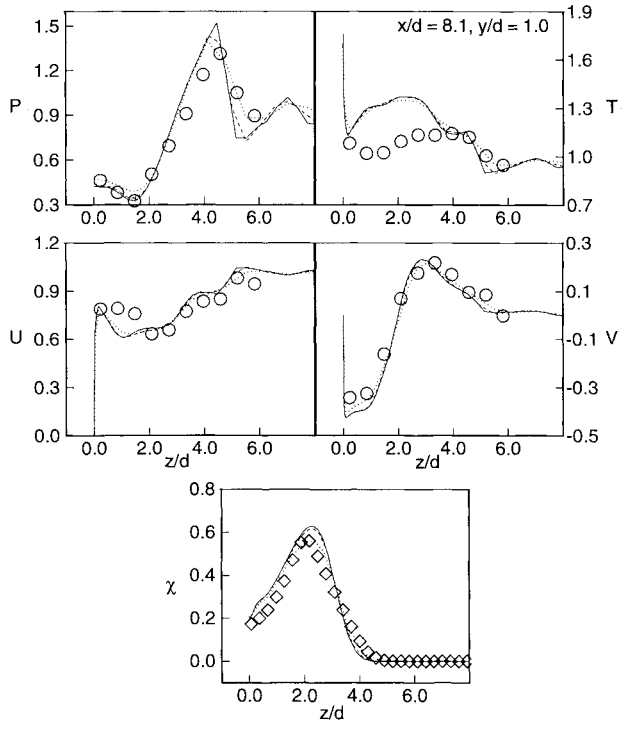

Fig. 9 Profiles of calculated values and pointwise LIIF measurements at $x/d = 8.1$, $y/d = 1.0$ (see Fig. 8 for the legend).

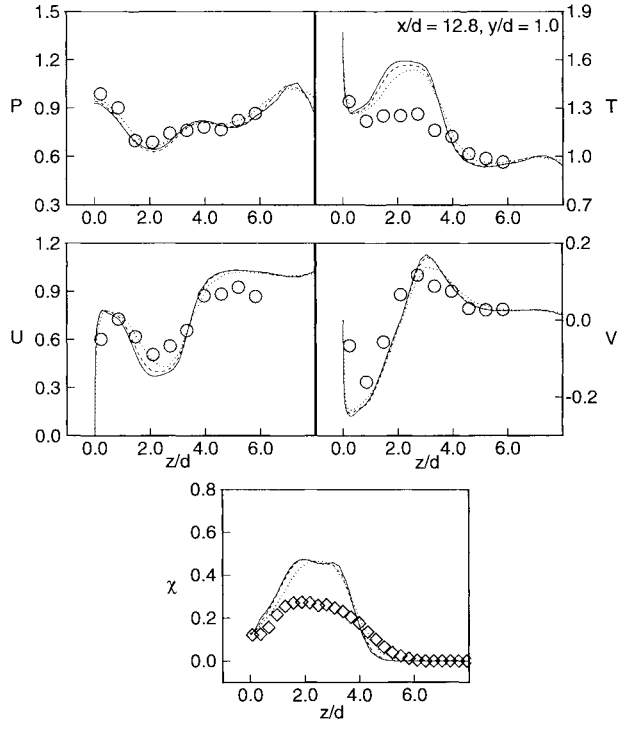

Fig. 10 Profiles of calculated values and pointwise LIIF measurements at $x/d = 12.8$, $y/d = 1.0$ (see Fig. 8 for legend).

Table 2 Mean difference for the staged injection flowfield

Solution	Pressure	Temperature	U Velocity	V Velocity	Mole fraction
Experimental uncertainty (%)[a]	± 4.0	± 2.0	± 5.0	± 4.0	± 1.5
(137 × 41 × 81) Grid	11.9 (36)	12.5 (18)	7.2 (47)	3.8 (68)	5.9 (24)
(103 × 31 × 61) Grid	11.7 (35)	12.7 (20)	7.4 (46)	3.8 (68)	6.1 (22)
(69 × 21 × 41) Grid	11.4 (35)	13.2 (22)	7.0 (54)	3.8 (67)	6.4 (26)

[a]In parenthesis are the percentage of values within the experimental accuracy limits.

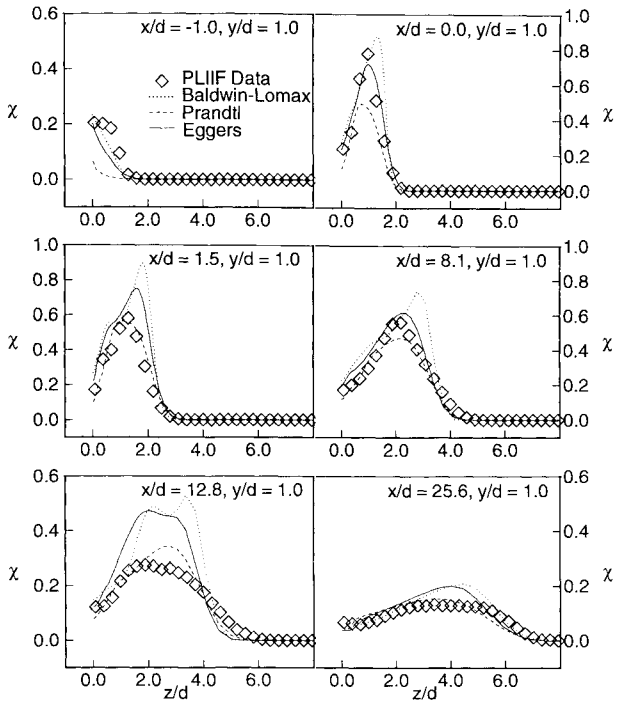

Fig. 11 Effect of the turbulence model on the mole fraction field at six locations.

is then obtained from the calculated and measured values according to

$$\bar{e} = \sum_{i=1}^{N} \frac{1}{N} \left| \frac{q_i^m}{q_\infty} - \frac{q_i^c}{q_\infty} \right| \tag{4}$$

where q is a particular flow property. Table 2 shows the mean difference values $\bar{e}$ obtained from the three calculated solutions and the LIIF data, augmented by the PLIIF mole fraction profiles. The 44 experimental locations are concentrated in the vicinity of the injectors; hence, $\bar{e}$ is dominated by this region. Only the experimental points with an absolute value greater than 0.01 were used to determine $\bar{e}$ for the mole fraction. This restriction prevented a large proportion of zero mole fraction values from artificially lowering $\bar{e}$. The values of $\bar{e}$ are highest for the temperature and pressure, which is partially due to the stronger shocks predicted in the calculations, the greater range of values in the flowfield for the nondimensional pressure, and the higher calculated temperatures in the core of the injectant.

Total Temperature Deficit

As was mentioned in the previous section, the total temperature inferred from the mean LIIF measurements is significantly lower than the reservoir value (1.8) at some locations. Recall, for instance, that T_0 inferred from the mean LIIF measurements equaled 1.37 and 1.46 at ($x/d = 1.5$, $y/d = 1.0$, $z/d = 0.86$) and ($x/d = 12.8$, $y/d = 1.0$, $z/d = 2.1$), respectively. The values of T_0 cited here were calculated from Eq. (3) by neglecting the normal component of velocity W and the components of the turbulent kinetic energy; u'^2, v'^2, and w'^2. Estimates of W can be drawn from the PLIIF data, and estimates of the turbulent kinetic energy can be drawn from the LDA data. LDA data were not obtained at ($x/d = 1.5$, $y/d = 1.0$) and ($x/d = 12.8$, $y/d = 1.0$), but they were obtained at ($x/d = 1.5$, $y/d = 0.0$) and ($x/d = 12.8$, $y/d = 0.0$). Hence, an estimate of u'^2 and w'^2 can be made, for example, at ($x/d = 1.5$, $y/d = 1.0$, $z/d = 0.86$) by selecting the maximum values obtained at ($x/d = 1.5$, $y/d = 0.0$). Also, an estimate of v'^2 can be made by choosing the maximum of either u'^2 or w'^2 at ($x/d = 1.5$, $y/d = 0.0$). The resultant combined contributions of W and the turbulent kinetic energy to the total temperature defined by Eq. (3) are only 0.06 at ($x/d = 1.5$, $y/d = 1.0$, $z/d = 0.86$) and 0.09 at ($x/d = 12.8$, $y/d = 1.0$, $z/d = 2.1$). Hence, the imbalance in T_0 inferred from the LIIF data is probably not solely attributable to the normal and fluctuating velocity components that were not measured with the LIIF technique.

Mechanisms for total temperature variation may include heat transfer, unsteady effects, and imbalance in viscous dissipation and heat conduction. Heat transfer through the walls, which were made of fused silica, was most likely very small, however, and would heat rather than cool the flow near the walls. Recent investigations have suggested that the unsteady nature of large scale vortical structures of a jet convecting downstream can cause nonuniformities in the total temperature distribution.[19,20] Fox et al.[19] measured the total temperature distribution of a freejet and an impinging jet with a total temperature of 298 K for Mach numbers ranging from 0.6 to 0.9. They found that nonuniformities in the total temperature increased with Mach number and for $M = 0.9$ equaled approximately 9 K or 4% of the freestream temperature for the freejet and approximately 28 K or 11% of the freestream temperature for the impinging jet. The dynamics of the unsteady nature of the vortices generated by the jets was not modeled because the calculations provided only the steady-state solution to the Reynolds-averaged Navier-Stokes equations. Finally, energy loss through the walls in the form of acoustic radiation, generated by flowfield unsteadiness in the vicinity of the jets would also produce a lower T_0. The magnitude of the acoustic energy radiated from the flowfield was not measured, however, nor was the effect of radiative transfer of acoustic energy through the walls modeled in the calculations. The apparent deficit in the total temperature inferred from the measurements at some locations is an area for further investigation.

Effect of the Turbulence Model

Overall, the solutions on the medium and fine grids were quite similar. Hence, the effect of the turbulence model on the comparisons was investigated by calculating solutions on the medium grid using the Baldwin-Lomax and the Prandtl turbulence models. (No attempt was made to optimize the performance of the turbulence models by adjusting the constants in the models.) The solution using the Baldwin-Lomax model was marked by an uneven distribution of eddy viscosity and generally small values of eddy viscosity in the vicinity of the jets. This effect was not unexpected since the length scale is based on the distance from the wall. The eddy viscosity distributions from the solutions using the Prandtl and the Eggers

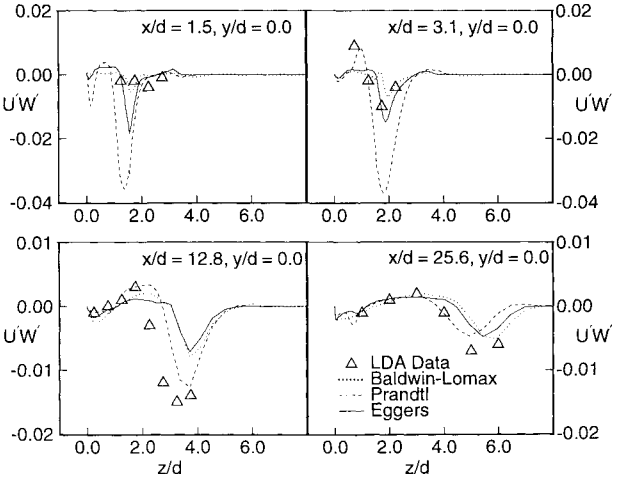

Fig. 12 Profiles of the nondimensional Reynolds stress $u'w'$ at four locations.

Table 3 Effect of turbulence model on mean difference

Solution	Pressure	Temperature	U Velocity	V Velocity	Mole fraction
Experimental uncertainty (%)[a]	± 4.0	± 2.0	± 5.0	± 4.0	± 1.5
Baldwin-Lomax model	13.5 (31)	12.1 (18)	8.2 (45)	4.3 (65)	8.2 (25)
Eggers model	11.7 (35)	12.7 (20)	7.4 (46)	3.8 (68)	6.1 (22)
Prandtl model	12.8 (27)	13.1 (18)	6.2 (53)	3.8 (68)	5.2 (27)

[a]In parenthesis are the percentage of values within the experimental accuracy limits.

mixing length models more closely tracked the injectant flow.[7] The solution using the Prandtl model had the largest values of eddy viscosity and hence the highest turbulent diffusion. This solution was generally found to more closely match the level of turbulent mixing found in the measurements as illustrated in Fig. 11, which shows the mole fraction profiles one diameter away from the centerline at six x/d locations. The sensitivity of the mole fraction values to the turbulence model in the near field of the injectors, as exhibited in Fig. 11, was larger than expected. Figure 12 shows the calculated and measured Reynolds stress, $u'w'$, along the centerline of the test section at four x/d locations. The Reynolds stress is obtained from the calculations according to the Boussinesq relation:

$$\rho u'w' = -\mu_t \left(\frac{\partial U}{\partial z} + \frac{\partial W}{\partial x} \right) \tag{5}$$

The Reynolds stress in Fig. 12 has been nondimensionalized by U_∞^2. Figure 12 shows significant variation in the calculated $u'w'$, especially in the near field of the injectors. The large variation in the calculated turbulence fields is consistent with the relatively large differences observed in the mean mole fraction profiles.

Table 3 shows the values of the mean difference $\bar{e}$ for the three turbulence treatments. The largest range in the values of $\bar{e}$ is for the mole fraction, which is due to the greater sensitivity of the mole fraction field to the calculated levels of eddy viscosity. While the mole fraction field was most sensitive to the turbulence model, significant differences in the velocity, pressure, and temperature fields were also observed between the three solutions. Although the mole fraction values from the solution obtained using the Prandtl model are in closer accord with the measured mole fractions, overall agreement with the entire data set was judged superior for the solution using the Eggers turbulence model.

Effect of the Jet Exit Conditions

As was previously mentioned, the Mach number at the exit of the jets has been a source of uncertainty. The characterization of the injector exit plane conditions is both important to the modeling of the flowfield, especially in the near field of the injectors, and very difficult experimentally. The experimental difficulty is due primarily to the extremely large gradients in the flow properties near the exit of the injector where strong expansion wave systems are located. A very small positioning error or spatial averaging effect due to the size of the measurement volume can cause large differences in the measured exit conditions. Original pointwise LIIF measurements of the pressure and temperature near the center of the jet indicated that the Mach number (assuming isentropic conditions) at the jet exit centerline was 1.35 (Ref. 21). This exit Mach number was used in the calculations presented so far. However, subsequent measurements at $z/d = 0.01$ along the extent of the injector in the streamwise direction indicated a strong streamwise variation in the exit Mach number. Separating a region of greater expansion on the downstream edge of the jet ($M = 2.0$) and a region of lesser expansion on the upstream edge of the jet ($M = 1.54$) was a relatively uniform region ($M = 1.32$) in the central portion of the injector. Later, measurements of the Mach number along the centerline of the injectors were deduced from the planar temperature measurements and from the LDA velocity measurements. The PLIIF and LDA measurements indicated that the injectors were essentially sonic at their exit planes.[2]

The effect on the comparisons of the assumed jet exit conditions was investigated. Calculations were obtained by assuming sonic flow at the jet exit and also by letting the Mach number vary linearly from sonic at the center of the jet to 1.5 at the edge of the jet. (The area of the injector was adjusted in both cases to maintain the nominal mass flow rate.) Both of these calculations were performed using the Eggers turbulence model on the coarse grid. This grid was chosen to minimize the resources required. However, changes in the jet exit conditions (and hence the modeled area of the injector) were also expected to have the largest effect upon solutions on the coarse grid. Comparisons of the mole fraction profiles at four streamwise locations, one diameter away from the centerline, obtained from the three solutions with different jet exit conditions are displayed in Fig. 13. Changes in the exit Mach number (and the modeled area of the injector) are more pronounced in the vicinity of the jets, as expected. The differences in the profiles are visible at the first location, but are barely discernible at the succeeding downstream locations. Generally, the injectant is found to penetrate slightly farther into the freestream in the original solution ($M = 1.35$), as expected, due to its larger jet momentum. (Note that the momentum of the jet is maximized when $M = \sqrt{2}$.) Overall, the effect on the comparisons due to the uncertainty in the Mach number at the exit of the jet is small.

Recapitulating, the turbulence models were found to have the greatest effect on the numerical solutions, followed by the grid resolution and the assumed jet exit Mach number. Similarly, the sources of error in the numerical solutions, in order of importance, are believed to be turbulence models, including not modeling the effects of any large scale unsteadiness, grid resolution and the lack of grid adaptation to the flow features, and the jet model, including the uncertainty in Mach number, the omission of a boundary layer, and the fidelity of the modeled circular geometry at the exit of the jet.

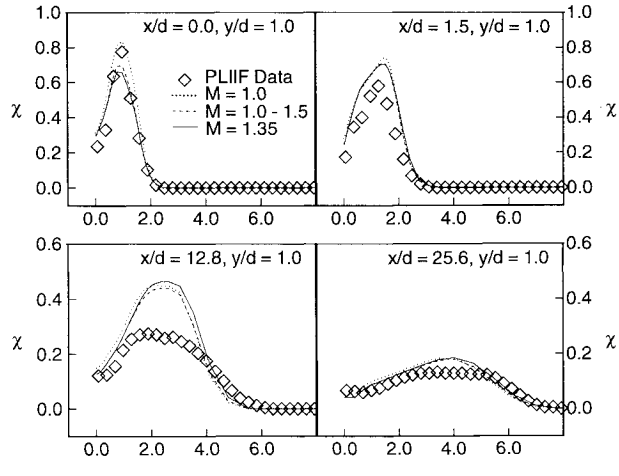

Fig. 13 Effect of the jet exit Mach number on the mole fraction field at six locations.

Conclusions

An extensive data set for the staged injection of two jets of air into a Mach 2 freestream behind a step has been acquired using LIIF and LDA measurement techniques. A companion numerical study was performed using the SPARK Navier-Stokes code. Because of the large quantity of data, a statistical measure was used to help assess agreement between the measurements and the calculations.

Comparisons between the calculations and the planar measurements exhibited good agreement in the mole fraction and velocity fields for this complex, highly three-dimensional flowfield. The mixing between the injectant and the freestream observed in the measurements was more rapid than predicted in the calculations, however, especially in the near field of the injectors. Comparisons of pressure along the centerline plane showed good agreement regarding the position of the prominent flow features: e.g., the expansion fan, Mach disks, and bow shocks. Measurements of pressure in the vicinity of the shock waves indicated stronger calculated than measured shocks.

Agreement between the calculations and the measurements obtained with the pointwise LIIF technique, as exhibited in the profiles at particular locations and as expressed in the statistical measure of agreement, was good. Agreement concerning the position and strength of the pair of streamwise vortices generated by the jets was found to be particularly good. Discrepancies were observed in the immediate vicinity of the jets regarding the strength of the shock system (as reflected in the pressure and temperature profiles). Differences between the measured and calculated temperatures of the injectant persisted downstream of the jets. A deficit in the total temperature, inferred from the LIIF measurements, was observed at several locations, perhaps due to flow unsteadiness.

The effect of grid resolution was investigated by calculating solutions on grids of 60,000 points, 200,000 points, and 450,000 points. Differences in the solutions on the two finer grids were small, although the solutions were distinguishable. The effect of numerical diffusion was observed to increase the predicted mixing. The effect of turbulence modeling was investigated by calculating solutions with three different algebraic models for the jet turbulence. The solution with the highest eddy viscosity values (Prandtl model), was found to generally agree better with the extent of mixing exhibited in the measurements. However, the solution using the Eggers model was judged to exhibit the best overall agreement. Finally, the effect of the uncertainty in the Mach number at the exit of the jets was examined. Varying the Mach number of the jet from 1.0 to 1.35 had a negligible effect upon the comparisons. Overall, the turbulence models were found to have the greatest effect upon the numerical solutions, followed by the grid resolution and the injectant Mach number.

The agreement observed between the nonintrusive, in situ measurements and the calculations is an important step both in validating the SPARK computer code and in demonstrating the accuracy of LIIF measurement techniques. Experience and confidence gained in modeling three-dimensional, turbulent mixing flowfields with the SPARK computer code will assist future efforts in modeling combustor flowfields with chemical reactions.

Acknowledgments

The computational work was supported in part by the National Research Council. The use of the computing facilities at the Numerical Aerodynamic Simulation (NAS) Program is also gratefully acknowledged. The experimental effort was supported at the University of Virginia under NASA grants NAG-1-373 and NAG-1-795 and at Virginia Polytechnic Institute and State University under NASA contract NAS1-18471. The authors would like to thank Glenn Diskin and Peter Jacobs for many helpful discussions during the course of this work and Steve Hollo for his help in formatting the experimental data set. The work of Roger Jones in preparing one of the figures is appreciated.

References

[1]Uenishi, K., Rogers, R. C., and Northam, G. B., "Numerical Predictions of a Rearward-Facing-Step Flow in a Supersonic Combustor," *Journal of Propulsion and Power,* Vol. 5, No. 2, 1989, pp. 158–164.

[2]McDaniel, J. C., Fletcher, D. G., Hartfield, R. J., and Hollo, S. D., "Staged Transverse Injection Into Mach 2 Flow Behind a Rearward-Facing Step: A Three-Dimensional Compressible Test Case for Hypersonic Combustor Code Validation," AIAA Paper 91-5071, Dec. 1991.

[3]Fletcher, D. G., and McDaniel, J. C., "Quantitative Characterization of a Nonreacting, Supersonic Combustor Using Laser-Induced Iodine Fluorescence," AIAA Paper 89-2565, July 1989.

[4]Hartfield, R. J., Abbitt, J. D., and McDaniel, J. C., "Injectant Mole-Fraction Imaging in Compressible Mixing Flows Using Planar Laser-Induced Iodine Fluorescence," *Optics Letters,* Vol. 14, No. 16, 1989, pp. 850–852.

[5]Hartfield, R. J., Hollo, S. D., and McDaniel, J. C., "Planar Measurement Technique for Compressible Flows Using Laser-Induced Iodine Fluorescence," *AIAA Journal,* Vol. 31, No. 3, 1993, pp. 483–490.

[6]Dancey, C. L., and Wang, J. A., "Laser Doppler Measurements in a Mach 2 Flow over a Rearward Facing Step with Staged Injection," Final Rept., NASA Contract NAS1-18471, Task No. 32, 1991.

[7]Eklund, D. R., Northam, G. B., and Fletcher, D. G., "Validation Study of the SPARK Navier-Stokes Code for Nonreacting Scramjet Combustor Flowfields," AIAA Paper 90-2360, July 1990.

[8]Eklund, D. R., Northam, G. B., McDaniel, J. C., and Smith, C., "Workshop Report: A Validation Study of Navier-Stokes Codes for Transverse Injection into a Mach 2 Flow," 29th JANNAF Combustion Meeting (Hampton, VA), Oct. 1992.

[9]Drummond, J. P., "A Two-Dimensional Numerical Simulation of a Supersonic, Chemically Reacting Mixing Layer," NASA TM-4055, Dec. 1988.

[10]Carpenter, M. H., "Three-Dimensional Computations of Cross-Flow Injection and Combustion in a Supersonic Flow," AIAA Paper 89-1870, June 1989.

[11]Carpenter, M., "A High Order Compact Numerical Algorithm for Supersonic Flows," *12th International Conference on Numerical Methods in Fluid Dynamics,* Springer Verlag, Berlin, 1990, pp. 254–258.

[12]Baldwin, B. S., and Lomax, H., "Thin Layer Approximation and Algebraic Model for Separated Turbulent Flows," AIAA Paper 78-257, Jan. 1978.

[13]Chitsomboon, T., Northam, G. B., Rogers, R. C., and Diskin, G. S., "CFD Prediction of the Reacting Flowfield Inside a Subscale Scramjet Combustor," AIAA Paper 88-3259, July 1988.

[14]Eggers, J. M., "Turbulent Mixing of Coaxial Compressible Hydrogen-Air Jets," NASA TN-D-6487, Sept. 1971.

[15]Riggins, D. W., Mao, M., Bittner, R. D., McClinton, C. R., and Rogers, R. C., "Numerical Modeling of Normal Fuel Injection, Effect of Turbulent Schmidt Number," NASP Rept., Ref. WBS 2.4.09, March 1989.

[16]Arnone, A., and Swanson, R. C., "A Navier-Stokes Solver for Cascade Flows," NASA CR-181682, July 1988.

[17]Heister, S., and Karagozian, A., "The Gaseous Jet in a Supersonic Crossflow," AIAA Paper 89-2547, July 1989.

[18]Glagolev, A. I., Zubkov, A. I., and Panov, Y. A., "Supersonic Flow Past a Gas Jet Obstacle Emerging from a Plate," *Mekhanika Zhidkosti i Gaza,* Vol. 2, No. 3, 1967, pp. 97–102.

[19]Fox, M., Kurosaka, M., and Hirano, K., "Total Temperature Separation in Jets," AIAA Paper 90-1621, June 1990.

[20]Hedges, L., and Eberhardt, S., "Numerical Simulation of Total Temperature Separation in Jets," AIAA Paper 92-0535, Jan. 1992.

[21]Fletcher, D. G., and McDaniel, J. C., "Laser-Induced Iodine Fluorescence Technique for Quantitative Measurement in a Nonreacting, Supersonic Combustor," *AIAA Journal,* Vol. 27, No. 5, 1989, pp. 575–580.